Magnetic resonance elastography of the brain: A comparison between pigs and humans

Johannes Weickenmeier[a,1], Mehmet Kurt[b,1], Efe Ozkaya[b], Max Wintermark[c], Kim Butts Pauly[c], Ellen Kuhl[d]

[a]*Department of Mechanical Engineering, Stanford University, Stanford, CA 94305, USA*
[b]*Department of Mechanical Engineering, Stevens Institute of Technology, Hoboken, NJ , USA*
[c]*Department of Radiology Stanford University Stanford, CA 94305, USA*
[d]*Departments of Mechanical Engineering and Bioengineering, Stanford University, Stanford, CA 94305, USA,*
email: ekuhl@stanford.edu, phone: +1.650.450.0855, fax: +1.650.725.1587, url: http:/biomechanics.stanford.edu, corresponding author
[1] *These authors contributed equally to this work.*

Abstract

Magnetic resonance elastography holds promise as a non-invasive, easy-to-use, in vivo biomarker for neurodegenerative diseases. Throughout the past decade, pigs have gained increased popularity as large animal models for human neurodegeneration. However, the volume of a pig brain is an order of magnitude smaller than the human brain, its skull is 40% thicker, and its head is about twice as big. This raises the question to which extent established vibration devices, actuation frequencies, and analysis tools for humans translate to large animal studies in pigs. Here we explored the feasibility of using human brain magnetic resonance elastography to characterize the dynamic properties of the porcine brain. In contrast to humans, where vibration devices induce an anterior-posterior displacement recorded in transverse sections, the porcine anatomy requires a dorsal-ventral displacement recorded in coronal sections. Within these settings, we applied a wide range of actuation frequencies, from 40 Hz to 90 Hz, and recorded the storage and loss moduli for human and porcine brains. Strikingly, we found that optimal actuation frequencies for humans translate one-to-one to pigs and reliably generate shear waves for elastographic post-processing. In a direct comparison, human and porcine storage and loss moduli followed similar trends and increased with increasing frequency. When translating these frequency-dependent storage and loss moduli into the frequency-independent stiffnesses and viscosities of a standard linear solid model, we found human values of $\mu_1 = 1.3$ kPa, $\mu_2 = 2.1$ kPa, and $\eta = 0.025$ kPa s and porcine values of $\mu_1 = 2.0$ kPa, $\mu_2 = 4.9$ kPa, and $\eta = 0.046$ kPa s. These results suggest that living human brain is softer and less viscous than dead porcine brain. Our study compares, for the first time, magnetic resonance elastography in human and porcine brains, and paves the way towards systematic interspecies comparison studies and ex vivo validation of magnetic resonance elastography as a whole.

Keywords: Magnetic resonance elastography; Human brain; Porcine brain; Storage and loss moduli; Viscoelasticity

1. Motivation

Magnetic resonance elastography was first proposed two decades ago [1, 2] and is rapidly gaining popularity as a non-invasive tool to measure the mechanical properties of living biological tissues [3]. To date, it remains the only in vivo measurement technique to characterize the mechanical properties of the living brain [4]. As such, it holds promise as a biomarker for the early onset of neurodegenerative diseases including multiple sclerosis [5] and Alzheimer's disease [6]. Several studies have used magnetic resonance elastography in small animals including rodents [7, 8, 9] and ferrets [10]. However, its application to larger animals remains challenging due to design constraints of the actuator and limited space inside the scanner. Despite its increasing interest and widespread use, magnetic resonance elastography is far from being fully validated. For example, recent studies have shown that its results are highly sensitive to the actuation frequency [11, 12]. Yet, the precise impact of tissue actuation on stiffness recordings remains insufficiently understood. In general, magnetic resonance elastography is based on three principles [3]: tissue actuation, the generation of shear waves through an external actuator; image acquisition, the recording of in vivo displacement fields based on a magnetic resonance sequence with motion-encoding gradients; and elastogram generation, the post-processing of phase-sensitive magnetic resonance images to create stiffness maps [4]. The objectives of this study are to use magnetic resonance elastography to characterize the viscoelastic properties of the porcine brain and to explore to which extent our recently developed protocols [11, 13] for tissue actuation, image acquisition, and elastogram generation translate from humans to pigs.

Tissue actuation. Most tissue actuators induce body waves that consist of compression and shear waves. While compression waves propagate at speeds of 1,500 m/s, shear waves are significantly slower and range from 1 to 10 m/s [14]. Current imaging sequences are fast enough to resolve the propagation of shear waves in soft tissues with wavelengths in the sub-millimeter to centimeter range [4]. Specialized magnetic resonance scanner-compatible actuators have been developed to characterize the stiffnesses of different organs under in vivo, in vitro, and ex vivo conditions. While the actual actuation device varies from study

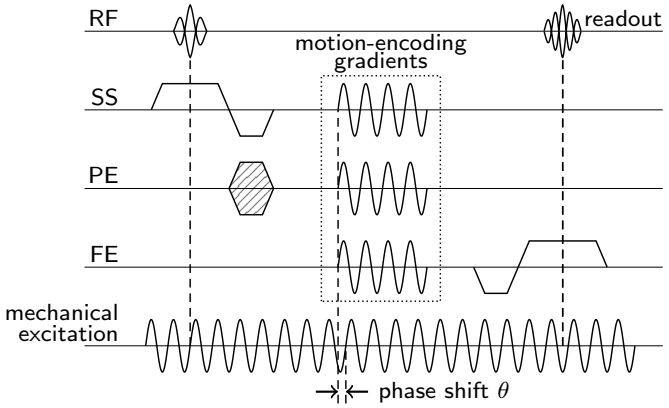

Figure 1: Magnetic resonance elastography is a phase-contrast based imaging technique that uses specialized sequences to image shear waves propagation. Synchronization of tissue activation through radio frequency (RF) pulses and motion-encoding gradients, slice-selection (SS), phase-encoded (PE), and frequency-encoded (FE) localization methods during image acquisition converts tissue motion into phase-sensitive images. A synchronization delay or phase shift θ between tissue activation and motion-encoding gradients allows us to capture tissue motion at distinct time points.

to study, the general setup aims at transmitting a low-frequency acoustic wave with frequencies smaller than 1 kHz using a sinusoidal mechanical source [15]. Frequency and wave source aim at inducing shear waves capable of penetrating the whole organ of interest and generating measurable wave amplitudes. Given the large variation in experimental setups and material properties, the optimal physiological range of vibration frequencies remains poorly understood [16, 11]. Especially in the case of the brain–a membrane-surrounded ultrasoft organ with multiple tissue interfaces and large local stiffness gradients [17]–the vibration frequency has a significant effect on wave reflection and interference, which can reduce displacement amplitudes and trigger wave dispersion [7].

Image acquisition. Magnetic resonance elastography is a phase-contrast based imaging technique [1]. It is based on the magnetic resonance imaging of shear wave propagation through specialized imaging sequences as illustrated in Fig. 1. The underlying paradigm is to synchronize a cyclic, gradient-based, oscillating magnetic field with the mechanical activation [2]. This causes spin packets, which move with the shear wave field inside the brain, to accrue phase during image acquisition. During each excitation period, we prescribe a locally varying gradient field. Individual spin packets move within this varying magnetic field and accumulate a different amount of phase [3]. Motion-encoding gradients cause the individual nuclear spin packets to accrue phase based on the local magnetic field strength as they oscillate with the gradients. As a result, the phase image of the data exhibits contrast proportional to displacement [7]. The phase shift of each position is received in the nuclear magnetic resonance signal and is aggregated in individual phase-sensitive magnetic resonance images. By introducing a synchronization delay between mechanical activation and motion-encoding gradient, we can capture displacement fields at distinct time points throughout each excitation period. Acquiring an image slice throughout several wave cycles allows us to accrue more phase and to determine an average tissue response at a local resolution of up to 100 nm [4]. By applying oscillating gradients of constant amplitude, frequency, and duration in three orthogonal directions, we can obtain the vector of motion-induced phase at each voxel in the image space and reconstruct the three-dimensional deformation field of the shear wave [7].

Elastogram generation. In linear elastic materials, harmonic elastography reconstructs the shear stiffness directly from shear speed estimates via the wave equation: The elastic shear modulus $G = \rho v$ is proportional to the tissue density ρ and the propagation speed $v = f\lambda$, the product of the actuation frequency f and the local wavelength λ of the propagating shear wave [4]. Assuming the density of the brain is equal to water, $\rho = 1\ \mathrm{g/cm^3}$, knowing the actuation frequency f, and measuring the local wavelength λ would allow us to directly extract the elastic modulus G. In more complex organs, however, measuring shear speed can be quite challenging. Using the Navier-Stokes equations [18], we can properly account for complex geometries and edge reflections given an appropriate discretization of the solution domain [19]. After acquiring phase-sensitive images in the region of interest, we can infer the displacement field based on a direct proportional relationship between phase and displacement magnitude. However, the ill-conditioned governing equations of displacements and material properties generate non-unique solutions, especially in the presence of experimental noise [19]. In addition, most soft tissues exhibit a frequency-dependent mechanical response [11], and often behave like nonlinear, anisotropic [20], viscoelastic [21] or poroelastic [22] solids. Following initially introduced simple, first-order direct inversion methods [1, 23], several groups have now introduced more accurate but computationally expensive continuum-model-based inversion schemes [15], including the time-of-arrival technique [24], sub-zone reconstruction [25], and coupled harmonic oscillator simulations [26]. Anisotropic inversion schemes remain challenging, but first efforts are underway to incorporate directionality of brain tissue stiffness into existing inversion algorithms [27].

2. Materials and methods

2.1. Subjects and samples

This study was approved by the Research Compliance Office at Stanford University and complies with IRB and Animal Care and Use guidelines. We received a 55 kg American Yorkshire pig 16 hours post-mortem, which had been cooled over night at 4°C. We removed the animal from the refrigerator three hours prior to scanning to minimize tissue degradation and changes in brain microstructure while allowing for the carcass to reach room temperature by the time of the scan. We compared the pig scan against our normal adult magnetic resonance elastography dataset obtained by using the same multi-frequency magnetic resonance elastography protocol [11]. This dataset contains a total number of $n = 51$ adult brains, 24 male and 27 female, aged between 18-80, with an average age of 44.5 years.

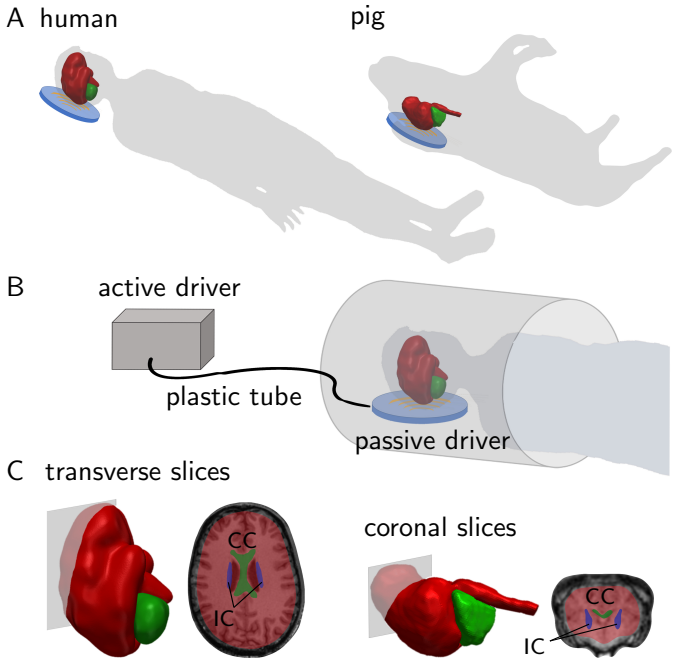

Figure 2: Magnetic resonance elastography. A. Human and porcine subjects are scanned in the supine position. B. The skull is accelerated through an active driver that is connected via a plastic tube to the passive driver pillow underneath the subject's head. C. The supine position of both subjects results in different imaging planes– transverse slices for humans and coronal slices for pigs.

2.2. Magnetic resonance imaging

Magnetic resonance imaging scans were performed on a 3T research scanner (GE Healthcare, Waukesha, WI) at the Richard M. Lucas Center for Imaging at Stanford University. Humans and the pig were scanned in the supine position, as shown in Fig. 2A. The anatomical orientation of the brains inside the scanner generated different scanning planes–transverse for humans and coronal for pigs–as illustrated in Fig. 2C. For the human brain, we used a 32-channel head coil and acquired 48 slices with 3 mm thickness at a matrix size of 128 × 128 with 1.875 mm resolution. For the porcine brain, we used a single-channel split head coil to accommodate the larger head and acquired 60 slices with 1.5 mm thickness at a matrix size of 128 × 128 with 1.25 mm resolution. Our scanning sequence designed for this study involved a T1-weighted anatomical scan, 3D-Bravo. Figures 3A and 4A show representative transverse, coronal, and sagittal slices of the human and pig brains.

2.3. Magnetic resonance elastography

Magnetic resonance elastography was performed using commercially available hardware and software in combination with the activation pillow developed and provided by courtesy of the Mayo Clinic (Mayo Clinic, Rochester, MN). An acoustic passive driver was placed underneath the subject's head, as shown in Fig. 2B. The driver was connected to an external acoustic active driver through a plastic tube. Continuous vibrations at a chosen frequency were generated by the active driver and delivered by the tube to the passive driver. These vibrations were then transmitted to the skull to induce shear waves inside the brain. We used a two-dimensional gradient echo (GRE) magnetic resonance elastography pulse sequence with repetition time (TR) 2s, echo time (TE) min full, matrix size 128×128, and field of view (FOV) 160×160 mm. Motion-sensitizing gradients encode the motion in the brain tissue into the phase of the magnetic resonance signal in three directions. We repeated the sequence eight times and acquired two phase images per location. To calculate the elastograms from the magnetic resonance elastography data, we used a two-dimensional direct inversion technique [23]. We chose four different vibration frequencies of the magnetic resonance elastography actuator, 40, 60, 80, and 90Hz. In each scan, we set the frequency of the motion encoding gradient equal to the actuation frequency for synchronization. For each actuation frequency, we determined maps of the storage and loss moduli.

Figures 3C and 4C show magnetic resonance measurements of the storage and loss moduli across a representative transverse slice in humans and coronal slice in pigs. The vibration pillow used in this study, together with the shape of the porcine head, only allows for tissue activation in the coronal plane. The triangular porcine skull provides an effective surface to induce tissue motion on the superior side of the head. In the supine position, the pig's head can be aligned well with the vibration pillow as shown in Fig. 2A.

2.4. Anatomical reconstruction of the brain

Anatomic reconstruction was performed using Simpleware (Synopsys, Mountain View, USA). From the T1-weighted magnetic resonance images, we reconstructed the anatomy and created three-dimensional models. Based on greyscale thresholding for an initial approximation of both structures, we applied manual segmentation and volumetric Gaussian smoothing to create the final three-dimensional models.

Figures 3B and 4B illustrate the volumetric representation of an adult male human brain and the pig brain. Human and porcine brains displayed distinct anatomic differences including the alignment of cerebrum and cerebellum and the shape and orientation of the brainstem. The human cerebral volume was eight times larger than the porcine cerebral volume; the human cerebellar volume was nine times larger than the porcine cerebellar volume.

2.5. Storage and loss moduli

To calculate average storage and loss moduli, we analyzed mid-coronal slices of the porcine brain. To capture average moduli, we selected gray and white matter regions as regions of interest and recorded the corresponding mean storage and loss moduli. For humans, we used segmentation templates that allow for an automated, region-specific parameter extraction [11]. For the pig, we manually segmented the corpus callosum and the internal capsule from the T1-weighted magnetic resonance images, see Fig. 2. We report the means and standard deviations of the storage and loss moduli G' and G'' for all four actuation frequencies, at 40, 60, 80, and 90 Hz.

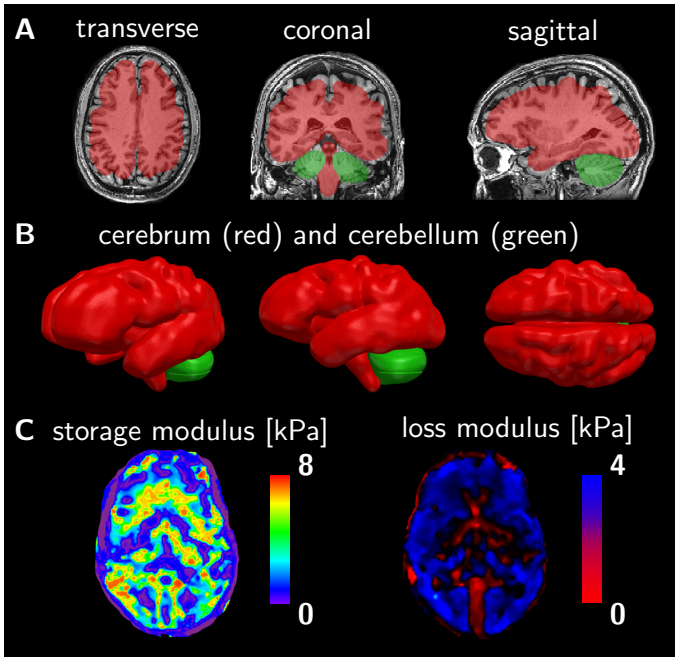

Figure 3: Human brain. A. Semi-automatic segmentation of the cerebrum and the cerebellum in transverse, coronal, and sagittal slices of the T1-weighted structural scan. B. Three-dimensional, lateral, and axial views of the volumetric reconstruction. C. Storage and loss moduli across a selected transverse section.

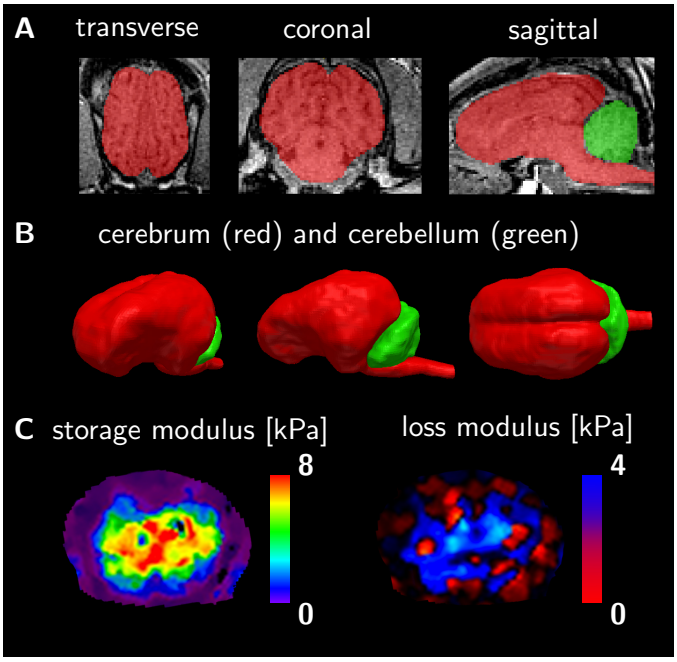

Figure 4: Porcine brain. A. Semi-automatic segmentation of the cerebrum and the cerebellum in transverse, coronal, and sagittal slices of the T1-weighted structural scan. B. Three-dimensional, lateral, and axial views of the volumetric reconstruction. C. Storage and loss moduli across a selected coronal section.

2.6. *Viscoelastic models*

To correlate the frequency-dependent storage and loss moduli G' and G'' to frequency-independent material parameters, we consider four commonly used viscoelastic models: the Maxwell model, the Voigt model, the spring-damper model, and the standard linear solid model. For each model, we express the model parameters in terms of the dynamic shear modulus $G = G' + iG''$. The Maxwell model mimics the serial arrangement of a spring and a damper with a stiffness μ and a viscosity η, which are related to the dynamic shear modulus as $G = (i\,\omega\,\eta\,\mu)/(\mu + i\,\omega\,\eta)$. The Voigt model mimics the parallel arrangement of a spring and a damper with a stiffness μ and a viscosity η, which are related to the dynamic shear modulus as $G = \mu + i\,\omega\,\eta$. The spring-damper model represents a combination of springs and dampers with a stiffness κ and an exponent α related to the dynamic shear modulus as $G = \kappa\,(i\omega)^{\alpha}$. The standard linear solid model consists of a spring with a stiffness μ_1 arranged parallel to a spring and damper with a stiffness μ_2 and a viscosity η related to the dynamic shear modulus as $G = (\mu_1\,\mu_2 + i\,\omega\,\eta\,(\mu_1 + \mu_2))/(\mu_2 + i\,\omega\,\eta)$. Figure 5 illustrates the relations between the frequency-independent elastic shear stiffness μ_1, viscoelastic shear stiffness μ_2, and viscosity η and the frequency-dependent storage and loss moduli G' and G'' for the standard linear solid model. For all four viscoelastic models, in each region of interest, we minimized the objective function

$$\Phi = \frac{1}{8}\left[\sum_{i=1}^{4}\left(\frac{G_i'^{\mathrm{exp}} - G_i'^{\mathrm{mod}}}{G_i'^{\mathrm{exp}}}\right)^2 + \left(\frac{G_i''^{\mathrm{exp}} - G_i''^{\mathrm{mod}}}{G_i''^{\mathrm{exp}}}\right)^2\right]^{1/2},$$

as the normalized root mean square error between the experimentally measured storage and loss moduli $G_i'^{\mathrm{exp}}$ and $G_i''^{\mathrm{exp}}$

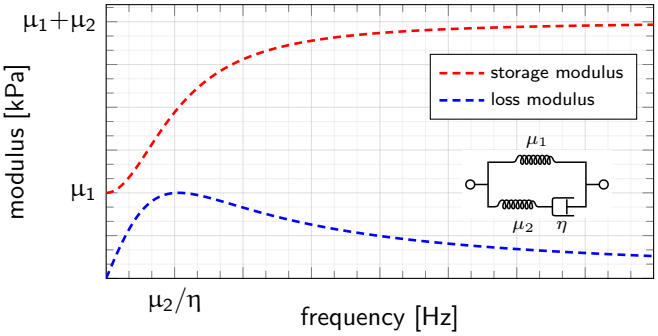

Figure 5: Standard linear solid model. Relations between frequency-independent elastic shear stiffness μ_1, viscoelastic shear stiffness μ_2, and viscosity η and frequency-dependent storage and loss moduli G' and G''. The storage modulus is $G' = \mu_1$ for frequencies $\omega \to 0$ and $G' = \mu_1 + \mu_2$ for frequencies $\omega \to \infty$. The loss modulus G'' is largest at the frequency ω associated with the inverse relaxation time $1/\tau = \mu_2/\eta$.

and the storage and loss moduli of $G_i'^{\mathrm{mod}}$ and $G_i''^{\mathrm{mod}}$ of the corresponding model summed over all four driver frequencies, $i = 40, 60, 80, 90$ Hz, using the Nelder-Mead method. To verify the robustness of the parameter identification, we screened the physically-motivated parameter space and performed the optimization with 17,500 different initial conditions for stiffnesses within the range of $\mu = 0.5$-8.0 kPa and viscosities of $\eta = 0.01$-1.00 kPa s.

3. Results

3.1. *Human and porcine loss and storage moduli G' and G''*

Table 1 summarizes the means and standard deviations of the storage and loss moduli G' and G'' for the human and porcine

brains at all four driver frequencies of 40, 60, 80, and 90 Hz. In general, our measurements were highly robust with low standard deviations ranging from 5% to 18%, with the exception of two loss moduli that displayed standard deviations of 35% and 40%. Both human and porcine moduli displayed similar trends and increased with increasing frequency. In the interval from 40 Hz to 90 Hz, the average human storage modulus increased from $G' = 1.182 \pm 0.127$ kPa to $G' = 2.224 \pm 0.160$ kPa and the average porcine storage modulus increased from $G' = 1.727 \pm 0.093$ kPa to $G' = 3.757 \pm 0.264$ kPa. At all four frequencies, the dead porcine brain was stiffer than the living human brain: The average porcine storage and loss moduli were 53% and 123% larger than their human counterparts.

Table 1: Storage and loss moduli G' and G'' for human and porcine brains at varying driver frequencies. Means and standard deviations from averaging over all n = 51 human brains and over all pixels across the pig brain.

	freq [Hz]	40	60	80	90
human	G' [kPa]	1.182 ± 0.127	1.893 ± 0.125	2.277 ± 0.137	2.224 ± 0.160
	G'' [kPa]	0.631 ± 0.218	0.941 ± 0.129	1.140 ± 0.179	0.987 ± 0.182
porcine	G' [kPa]	1.727 ± 0.093	2.591 ± 0.378	3.546 ± 0.198	3.757 ± 0.264
	G'' [kPa]	1.233 ± 0.207	2.211 ± 0.885	2.288 ± 0.232	2.534 ± 0.164

Figure 6 shows the frequency-dependent, region-specific storage and loss moduli G' and G'' for the porcine and human brains. In addition to the average brain values from Table 1 in Fig. 6A, we also summarize the regional moduli of two characteristic deeper brain structures, the corpus callosum in Fig. 6B and the internal capsule in Fig. 6C. Both human and porcine storage and loss moduli of the corpus callosum and the internal capsule displayed similar trends to the overall brain average in Fig. 6A. Human and porcine storage moduli in all three regions increased with increasing frequency from 40 Hz to 80 Hz. Counterintuitively, in the corpus callosum and the internal capsule, both human and porcine storage moduli decreased from 80 Hz to 90 Hz. Overall, all three graphs in Fig. 6 confirm the general trend of Table 1: In all three regions, both storage and loss moduli of the dead porcine brain were markedly larger than the storage moduli of the living human brain.

3.2. Comparison of viscoelastic models

Table 2 summarizes the rheological models, the functional relations, and the parameters of our four viscoelastic models, Maxwell, Voigt, spring-damper, and standard linear solid, for three regions, brain average, corpus callosum, and internal capsule of the porcine brain. For each model and region, we also report the normalized root mean square error between the experimental moduli G'^{exp} and G''^{exp} and the moduli predicted by the model G'^{mod} and G''^{mod}. For the Maxwell, Voigt, and spring-damper models, the parameter identification robustly identified

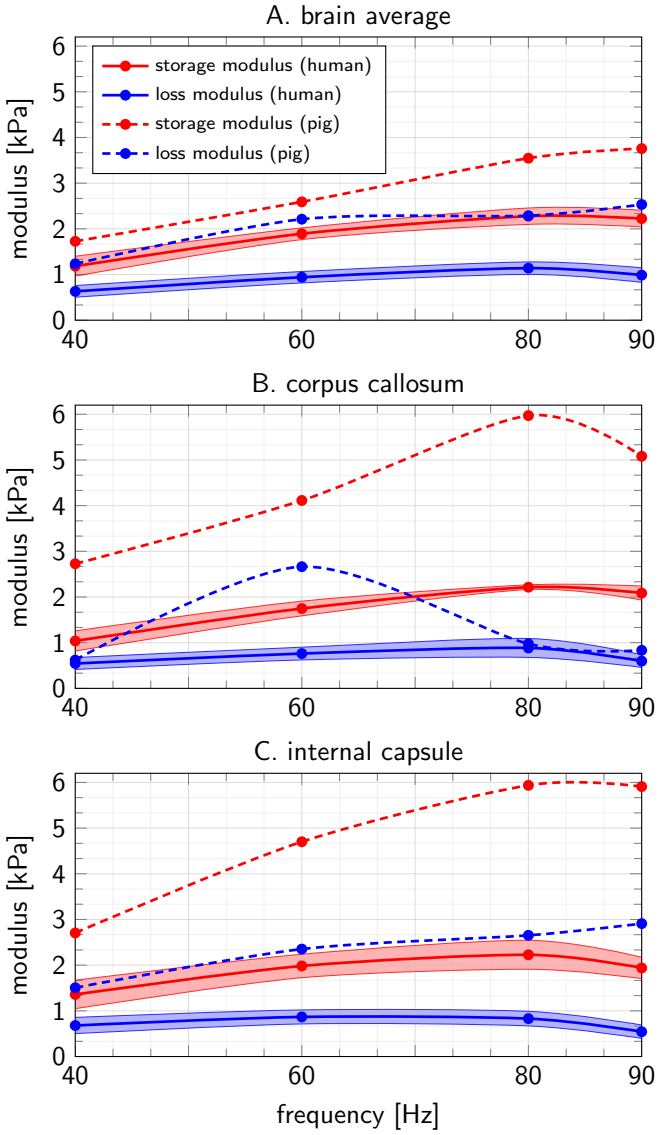

Figure 6: Storage and loss moduli G' and G'' for human and porcine brains at varying driver frequencies. Region-specific moduli for A. brain average, B. corpus callosum, and C. internal capsule. Dashed lines indicate mean pig moduli, solid lines indicate mean human moduli averaged over n = 51 adult brains, and shaded regions indicate their standard deviations.

the same minimizing parameter sets for varying initial conditions. For the standard linear solid model, the parameter identification was sensitive to the set of initial conditions, particularly because of the limited number of frequencies tested in this study. Eventually, we selected the parameter set with the lowest normalized root mean square error. In summary, all four models performed well with errors smaller than 33% in any of the three regions. Shear stiffnesses generally ranged from $\mu = 2.0$ kPa to $\mu = 6.3$ kPa, with smaller values for the overall brain average and larger values for the corpus callosum and the internal capsule. Of all three regions, all models displayed the largest error for the corpus callosum, most likely caused by the unexpected sudden reduction in storage modulus from 80 to 90 Hz, see Fig. 6B. Of all four rheological models, the Maxwell model displayed the largest relative errors, 11% for brain av-

Table 2: Viscoelastic models. Rheological models, functional relations, and parameters of Maxwell model, Voigt model, spring-damper model, and standard linear solid model determined from frequency-dependent storage and loss moduli G' and G'' of the porcine brain. Region-specific parameters for brain average (BA), corpus callosum (CC), and internal capsule (IC) and normalized root mean square errors between experimentally measured moduli and moduli predicted by the four models.

porcine	Maxwell model			Voigt model			spring-damper model			standard linear solid model			
	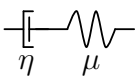 $G = \frac{i\omega\eta\mu}{\mu + i\omega\eta}$			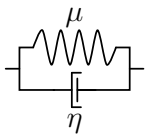 $G = \mu + i\omega\eta$			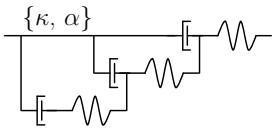 $G = \kappa(i\omega)^{\alpha}$			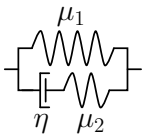 $G = \frac{\mu_1\mu_2 + i\omega\eta(\mu_1 + \mu_2)}{\mu_2 + i\omega\eta}$			
region	μ [kPa]	η [kPa s]	err [–]	μ [kPa]	η [kPa s]	err [–]	κ [kPa]	α [-]	err [–]	μ_1 [kPa]	μ_2 [kPa]	η [kPa s]	err [–]
BA	4.795	0.088	0.110	2.905	0.030	0.097	0.660	0.407	0.076	2.001	4.949	0.046	0.081
CC	5.020	0.222	0.325	4.473	0.017	0.165	2.090	0.194	0.201	2.163	4.000	0.086	0.321
IC	6.362	0.169	0.149	4.813	0.034	0.105	1.503	0.308	0.090	2.160	5.524	0.068	0.072

erage, 33% for the corpus callosum, and 15% for the internal capsule, suggesting that it is poorly suited to characterize the viscoelastic behavior of brain tissue. The standard linear solid model displayed the smallest relative error, 7% for the internal capsule. Of all four models, the standard linear solid model is the only model that features an instantaneous stiffness at vanishing frequencies and a non-linear frequency dependency at a non-zero steady state. We therefore selected the standard linear solid model for a direct comparison between the viscoelastic parameters of human and porcine brains.

3.3. Human and porcine stiffnesses μ_1 and μ_2 and viscosities η

Table 3 compares the elastic and viscoelastic shear moduli μ_1 and μ_2 and the viscosity η of the standard linear solid model according to Fig. 5 of human and porcine brains. The frequency-independent parameters for the brain average, corpus callosum, and internal capsule displayed marked differences between the living human and dead pig brain. Overall, the parameters of the porcine brain were about twice as large as those of the human brain. The elastic stiffness of the porcine brain $\mu_1 = 2.001$ kPa was by a factor 1.6 larger than the elastic stiffness of the human brains $\mu = 1.261$ kPa when averaged over the entre brain, and it was 1.7 times larger in the corpus callosum and 2.2 times larger in the internal capsule. The viscoelastic stiffness μ_2 was also larger in all regions of the porcine brain than in the human brain, by a factor 2.4 for brain average, 2.6 in the corpus callosum, and 3.5 in the internal capsule. The viscosity η was also larger in all regions of the porcine brain than in the human brain, by a factor 1.8 for brain average, 3.7 in the corpus callosum, and 2.1 in the internal capsule. The average relaxation time $\tau = \eta/\mu_2$ of the living human brain of $\tau = 12.1$ ms was comparable to the average relaxation time of the dead porcine brain with $\tau = 9.3$ ms.

Table 3: Standard linear solid model. Elastic shear stiffness μ_1, viscoelastic shear stiffness μ_2, and viscosity η determined from frequency-dependent storage and loss moduli G' and G'' of human and porcine brains. Region-specific parameters for brain average (BA), corpus callosum (CC), and internal capsule (IC).

		standard linear solid model		
	region	μ_1 [kPa]	μ_2 [kPa]	η [kPa s]
human	**BA**	1.261	2.068	0.025
	CC	1.257	1.548	0.023
	IC	0.994	1.591	0.033
porcine	**BA**	2.001	4.949	0.046
	CC	2.163	4.000	0.086
	IC	2.160	5.524	0.068

4. Discussion

Magnetic resonance elastography is rapidly gaining popularity as a non-invasive, easy-to-use, in vivo technology to characterize regional stiffness variations across the living human brain. Yet, to be fully applicable for broad clinical use, the technique could benefit from a more thorough calibration and validation, both against other methods and against other species. To increase our confidence in the recordings, enable a comparison of measurements and experimental data, and calibrate and validate the technology, it seems intuitive to ask, how well it performs when applied to animal models. While several studies have applied magnetic resonance elastography to small animal models, including rats [28] and ferrets [10], the technique has never been applied to large animal models comparable to humans. Here we demonstrate, for the first time, the feasibility of magnetic resonance elastography to characterize the storage and loss moduli of a porcine brain in situ.

Scanning pigs presents several differences as compared to standard human scans. The dimensions of a porcine brain are about half of those of a human brain which implies that its vol-

ume and mass are an order of magnitude smaller than in humans. Our human brain was eight times larger in volume than the porcine brain, which agrees well with brain weights ranging from 1,300 to 1,500 g for humans versus 150 to 180 g for pigs [29]. To achieve the same image accuracy, the resolution of the scan would therefore have to be twice as high. At the same time, the overall pig head is almost twice as large as the human head. Its flesh mass alone is almost five times larger with 918.1 g for humans and 4,186 g for pigs [29], and its skull is about 40% thicker with 6.9 mm for humans and 9.7 mm for pigs [30]. The dimensions of the head and its orientation with respect to the rest of the body made it impossible to use the 32-channel head coil routinely used for humans and we had to use a single-channel split head coil instead. In view of the dynamic vibration, the larger head mass and smaller brain mass suggest that the optimal vibration frequencies for pigs should be markedly different from those for humans. Last, and probably more importantly, the pig anatomy suggests coronal scan and activation planes, while the human anatomy suggests transverse planes. Strikingly, with all these differences between pigs and humans, our study revealed that when scanned in the same supine position and at the same vibration frequencies as humans, pig scans provided reliable and comparable magnetic resonance elastography recordings with storage and loss moduli within the same range as humans.

4.1. Magnetic resonance elastography in humans vs. pigs

Several magnetic resonance elastography studies have developed specialized driver setups to induce sufficiently repeatable brain deformations in human [4] or small animal [10] brains. The objective of this study was to test the feasibility of using the driver hardware and accompanying imaging software originally developed for the human brain [31] on a large animal brain. We found that the supine scanning position of the animal enabled effective transfer of the driver displacement to the animal brain. In comparison to humans, for which the setup induces an anterior-posterior displacement recorded via images in the transverse plane [4], the porcine anatomy causes a dorsal-ventral displacement recorded via images in the coronal plane as illustrated in Fig. 2. This setup implied slightly different resolutions, 48 slices with 3 mm thickness at a matrix size of 128 $\times$ 128 with 1.875 mm resolution in humans and 60 slices with 1.5 mm thickness at a matrix size of 128 $\times$ 128 with 1.25 mm resolution in the pig, which could potentially impact the results. The different scan planes could also have an impact on the stiffness recordings since cerebral tissue–white matter in particular–displays a pronounced structural anisotropy. Recent ex vivo studies have shown though that the stiffnesses parallel and perpendicular to the fiber bundle orienation displayed no statistically differences, neither in humans [21] nor in pigs [32].

As part of this study, our goal was to establish a reliable magnetic resonance elastography protocol to record stiffness values of porcine brain. Our main parameter of interest was the actuation frequency ω of the vibrating pillow. For the porcine brain, we found that actuation frequencies lower than 40 Hz and higher than 90 Hz resulted in extremely small displacements and thus, large signal-to-noise ratios. Interestingly, in view of signal-to-noise ratio and phase generation, the optimal frequency regime for porcine brains between 40 Hz and 90 Hz highlighted in Table 1 and Fig. 6 was similar to that for human brains [11, 12].

For a quantitative evaluation, we compared the storage and loss moduli G' and G'' of average living human brains [11] with those of a dead pig. The general trends were strikingly similar: At any given frequency, the storage modulus was about 50-100% larger than the loss modulus, and both moduli increased with increasing frequency up to 80 Hz. Yet, the absolute values of the dead porcine brain were larger than those of the living human brain across both moduli and all frequencies. With respect to frequency sensitivity, both average human and porcine brain storage moduli increased with increasing frequency in agreement with human frequency sensitivity studies reported in the literature [12], and converged to peak values of $G' = 2.2$ kPa for humans and $G' = 3.6$ kPa for the pig at around 80 Hz.

In excellent agreement with the literature, we recorded average human brain storage and loss moduli of G'=1.18-2.22 kPa and G''=0.63-0.99 kPa for frequencies ranging from 40 to 90 Hz compared to previously reported values of G'=1.1-2.0 kPa and G''=0.48-0.80 kPa for slightly lower frequencies ranging from 25 to 62.5 Hz [12]. Our average human brain storage and loss moduli of G'=2.28 kPa and G''=1.14 kPa at 80 Hz agree well with previously reported storage and loss moduli of G'=2.41 kPa and G'=2.34 kPa for white matter and G''=1.21 kPa and G''=1.11 kPa for gray matter [33]. Our average pig brain storage and loss moduli of G'=1.73-3.86 kPa and G''=1.23-2.53 kPa for frequencies ranging from 40 to 90 Hz were 53% and 123% larger than in humans, but not as high as the reported values of G'=8.45 kPa and G''=7.14 kPa for a frequency of 180 Hz recorded in rats [28] and G'=3-7 kPa and G''=1-2 kPa for frequencies ranging from 400 Hz to 800 Hz recorded in ferrets [10]. Unfortunately, these small animal stiffnesses are difficult to compare to our large animal model values since we were unable to record reliable data for activation frequencies higher than 80 Hz due to limited excitation.

4.2. Comparison of viscoelastic models

In agreement with previous studies, our study confirms that the storage and loss moduli G' and G'' acquired through magnetic resonance elastography increase with increasing frequency [10, 11]. To convert these frequency-dependent parameters into frequency-independent parameters, we analyzed four common viscoelastic models [12]: the Maxwell model with an elastic spring and a viscous damper arranged in series, the Voigt model with a spring and damper arranged in parallel, the spring-damper model with several Maxwell models in parallel, and the standard linear solid model with an elastic spring in parallel to a Maxwell model. In general, that data from only four frequencies provides a rather limited information to identify the two or even three material parameters of these viscoelastic models. Nonetheless, our least square parameter identification was robust and stable and generally identified the same parameter set for varying initial values. The shear stiffnesses of all four models varied between $\mu = 2.0 - 4.8$ kPa for the dead porcine brain and were about twice as large as their human brain counterparts.

Of the four viscoelastic models, the Voigt model predicted a constant, frequency-independent storage modulus; the Maxwell and spring-damper models predicted a vanishing storage modulus under quasi-static conditions. Of all four models, only the standard linear solid model displayed a non-zero stiffness under quasi-static conditions and a non-linear frequency dependency. In the finite hyper-viscoelastic setting, the standard linear solid model generalizes to the popular multiplicative decomposition model with one viscoelastic mode [34]. Our stiffness values for the standard linear solid model of μ_1=1.3 kPa and μ_2=2.1 kPa in humans and μ_1=2.0 kPa and μ_2=4.9 kPa in the pig agree well with the stiffnesses previously reported for human brains of μ_1=1.0 kPa and μ_2=1.5 kPa [12]; however, our viscosities of η=0.025 kPa and η=0.046 kPa s were slightly higher than the previously reported value of η=0.004 Pa s. Our in vivo human brain stiffnesses of the standard linear solid model of μ_1=1.3 kPa and μ_2=2.1 kPa were of the same order as our previously reported ex vivo human brain stiffnesses of the finite hyper-viscoelastic model of μ_1=0.7 kPa and μ_2=2.1 kPa; however, our in vivo viscosity of of η=0.025 kPa s was markedly lower than the ex vivo viscosity of η = 20.0 kPa s [35].

4.3. Storage and loss moduli in vivo, in situ, and ex vivo

Soft biological tissues are highly sensitive to environmental factors and immediately change when diseased, dead, excised, or processed for experimental testing [36]. Especially the brain, which consumes an essential part of the body's energy, is one of the most perfused organs, and constantly pressurized, is likely to undergo tissue degradation in terms of autolytic processes, completion of rigor mortis, and osmotic swelling after death. When comparing the short-term stiffness of living porcine brain in vivo of 1.88 kPa to the stiffness shortly after death in situ of 2.80 kPa, and to the excised stiffness in vitro of 1.36 kPa, studies found an initial stiffness increase of 49% post mortem followed by a stiffness decrease of 49% upon excitation [37]. These findings agree with findings in rats, for which the storage modulus G' increased significantly by up to 100% immediately after death but returned to its initial value after 24 hours post mortem. At the same time, the loss modulus G'' remained the same immediately after death, but decreased by about 50% after 24 hours [38]. For longer post mortem times of up to 6 hours [39], 15 hours [40], 48 hours [41], and 100 hours [42], the storage modulus of porcine brains remained virtually constant with variations of 5% and less. These observations could explain why our average in situ human brain stiffnesses of μ_1=1.26 kPa and μ_2=2.07 kPa were larger than our previously measured in vitro human brain stiffnesses of μ_1=0.13-0.74 kPa and μ_2=0.91-1.60 kPa [35]. Similarly, our average in situ pig brain storage and loss moduli of G'=1.73-3.86 kPa and G''=1.23-2.53 kPa for frequencies ranging from 40 to 90 Hz were larger than the average in vitro moduli of G'=1.15-1.22 kPa and G''=0.91-1.07 kPa for frequencies ranging from 80 Hz to 140 Hz recorded for isolated pig brains [28]. Structural differences between living and dead tissues could explain why our recorded shear stiffness of the dead porcine brain in situ of μ_1 = 2.001 kPa was almost twice as large as the reported shear stiffness of the living brain in vivo of μ = 1,080 kPa [43]. Our porcine model is a valuable model system that would allow us to elaborate the origin of these discrepancies in more detail by making a direct comparison between living and dead tissue in one and the same brain.

4.4. Challenges and limitations

Our study demonstrates that established human magnetic resonance elastography protocols [11] can be directly applied to domestic pigs. Our findings are limited, however, by a number of aspects. First, our study was based on a single animal, scanned 16 hours post-mortem. Both factors have affected the magnitude of the recorded storage and loss moduli and impeded a direct comparison with the reported human data. Second, we chose similar imaging parameters for both human and pig which resulted in a coarser resolution for the smaller pig brain. Although three-dimensional digital brain atlases for domestic pigs exist [44], there are no automated segmentation tools for porcine brains. The reduced in-plane resolution complicated the semi-automatic segmentation and the selection of individual regions when determining region-specific storage and loss moduli. Third, for the lack of better knowledge, we have simply adapted existing inversion techniques for human brains to generate storage and loss moduli maps across the porcine brain. Previous human brain elastograms have revealed distortions at the dural folds and at the brain-skull interface [45], characteristic anatomic locations which are likely different in pigs. Fourth, by their very nature, the elastogram construction and parameter identification are based on the assumption of a linear material behavior. There is a general consensus that brain tissue is a hyper-viscoelastic material [46, 47]. It is also well accepted that the brain is stiffer in compression than in extension [48]. While brain tissue displays a significant nonlinear response under moderate deformations [35, 49, 50], our measured displacement fields were on the order of 10 μm, which agrees well with the displacement range reported in the literature [51]. Besides these small deformations, our elastography imaging sequence currently limits us to linear inversion schemes when calculating our elastograms. This suggests that a linear theorysymmetric in tension and compressionrepresents a reasonable first approximation for our current acceleration parameters and enables the identification of meaningful linear viscoelastic material parameters.

4.5. Clinical implications

Pigs have shown promising results as realistic animal models for neurodegenerative disorders and can provide insight into the pathophysiology of brain diseases including dementia [52]. Their similarity with humans in view of anatomy, myelination, gyrification, development, and quantifiable behavior traits promotes pigs as valuable animal models [53]. Most small animal models lack fundamental biochemical or genetic manifestations of neurodegenerative diseases in human, and are therefore insufficient to fully study these diseases. The porcine brain is currently explored as a more realistic alternative to test novel diagnostic tools and explore treatment strategies in neurodegeneration [54]. Towards these goals, our current study provides a first step to establish reliable data acquisition protocols and validate

magnetic resonance elastography as a non-invasive biomarker for stiffness changes in living human and porcine brains in vivo.

Acknowledgements

Johannes Weickenmeier and Ellen Kuhl were supported by the NSF grant CMMI 1727268 Understanding Neurodegeneration across the Scales. Mehmet Kurt was supported by the Stanford Child Health Research Institute and the Thrasher Research Foundation Early Career Award. We thank Richard L. Ehman from the Mayo Clinic Rochester for providing the activation device and acknowledge his support through the NIH grant EB001981. We acknowledge Karla Epperson, Kevin Epperson, and Anne M. Saywer from the Richard M. Lucas Center for Imaging at Stanford University for their support during the carcass measurements and John Martinez from Stevens Institute of Technology for his contributions to the data analysis. Scanning of human volunteers was supported by General Electric Healthcare Tiger Team funding.

References

[1] R. Muthupillai, D. Lomas, P. Rossman, J. F. Greenleaf, J. Greenleaf, R. Ehman, Magnetic resonance elastography by direct visualization of propagating acoustic strain waves, Science 269 (5232) (1995) 1854–1857.

[2] R. Muthupillai, R. Ehman, Magnetic resonance elastography, Nature Medicine 2 (5) (1996) 601–603.

[3] Y. K. Mariappan, K. J. Glaser, R. L. Ehman, Magnetic resonance elastography: a review, Clinical Anatomy 23 (5) (2010) 497–511.

[4] S. A. Kruse, G. H. Rose, K. J. Glaser, A. Manduca, J. P. Felmlee, C. R. Jack, R. L. Ehman, Magnetic resonance elastography of the brain, Neuroimage 39 (1) (2008) 231–237.

[5] K.-J. Streitberger, I. Sack, D. Krefting, C. Pfüller, J. Braun, F. Paul, J. Wuerfel, Brain viscoelasticity alteration in chronic-progressive multiple sclerosis, PloS one 7 (1) (2012) e29888.

[6] M. C. Murphy, J. Huston, C. R. Jack, K. J. Glaser, A. Manduca, J. P. Felmlee, R. L. Ehman, Decreased brain stiffness in Alzheimer's disease determined by magnetic resonance elastography, Journal of Magnetic Resonance Imaging 34 (3) (2011) 494–498.

[7] S. M. Atay, C. D. Kroenke, A. Sabet, P. V. Bayly, Measurement of the dynamic shear modulus of mouse brain tissue in vivo by magnetic resonance elastography, Journal of Biomechanical Engineering 130 (2) (2008) 021013.

[8] K. Schregel, E. Wuerfel, P. Garteiser, I. Gemeinhardt, T. Prozorovski, O. Aktas, H. Merz, D. Petersen, J. Wuerfel, R. Sinkus, Demyelination reduces brain parenchymal stiffness quantified in vivo by magnetic resonance elastography, Proceedings of the National Academy of Sciences 109 (17) (2012) 6650–6655.

[9] Y. Feng, E. Clayton, R. Okamoto, J. Engelbach, P. Bayly, J. Garbow, A longitudinal magnetic resonance elastography study of murine brain tumors following radiation therapy, Physics in Medicine and Biology 61 (16) (2016) 6121.

[10] Y. Feng, E. Clayton, Y. Chang, R. Okamoto, P. Bayly, Viscoelastic properties of the ferret brain measured in vivo at multiple frequencies by magnetic resonance elastography, Journal of Biomechanics 46 (5) (2013) 863–870.

[11] M. Kurt, H. Lv, K. Laksari, L. Wu, K. Epperson, K. Epperson, A. M. Sawyer, D. B. Camarillo, K. Butts Pauly, M. Wintermark, In vivo multi-frequency magnetic resonance elastography of the human brain: Which frequencies matter?, in: Biomedical Engineering Society Annual Meeting October 11-14, Phoenix, AZ, USA, 2017.

[12] I. Sack, B. Beierbach, J. Wuerfel, D. Klatt, U. Hamhaber, S. Papazoglou, P. Martus, J. Braun, The impact of aging and gender on brain viscoelasticity, Neuroimage 46 (3) (2009) 652–657.

[13] A. G. Chartrain, M. Kurt, A. Yao, R. Feng, K. Nael, J. Mocco, J. B. Bederson, P. Balchandani, R. K. Shrivastava, Utility of preoperative meningioma consistency measurement with magnetic resonance elastography (MRE): A review, World Neurosurgery (2017) in press; doi:10.1007/s10143–017–0862–8.

[14] M. A. Green, L. E. Bilston, R. Sinkus, In vivo brain viscoelastic properties measured by magnetic resonance elastography, NMR in Biomedicine 21 (2008) 755–764.

[15] M. Doyley, Model-based elastography: a survey of approaches to the inverse elasticity problem, Physics in Medicine and Biology 57 (3) (2012) R35.

[16] K. Laksari, L. C. Wu, M. Kurt, C. Kuo, D. C. Camarillo, Resonance of human brain under head acceleration, Journal of The Royal Society Interface 12 (108) (2015) 20150331.

[17] J. Weickenmeier, R. de Rooij, S. Budday, P. Steinmann, T. Ovaert, E. Kuhl, Brain stiffness increases with myelin content, Acta Biomaterialia 42 (2016) 265–272.

[18] S. Papazoglou, U. Hamhaber, J. Braun, I. Sack, Algebraic Helmholtz inversion in planar magnetic resonance elastography, Physics in Medicine and Biology 53 (12) (2008) 3147–3158.

[19] D. B. Plewes, J. Bishop, A. Samani, J. Sciarretta, Visualization and quantification of breast cancer biomechanical properties with magnetic resonance elastography, Physics in Medicine and Biology 45 (6) (2000) 1591–1610.

[20] M. Böl, A. E. Ehret, K. Leichsenring, M. Ernst, Tissue-scale anisotropy and compressibility of tendon in semi-confined compression tests, Journal of Biomechanics 48 (6) (2015) 1092–1098.

[21] S. Budday, G. Sommer, C. Langkammer, J. Hayback, J. Kohnert, M. Bauer, F. Paulsen, P. Steinmann, E. Kuhl, G. Holzapfel, Mechanical characterization of human brain tissue, Acta Biomaterialia 48 (2017) 319–340.

[22] G. Franceschini, D. Bigoni, P. Regitnig, G. A. Holzapfel, Brain tissue deforms similarly to filled elastomers and follows consolidation theory, Journal of the Mechanics and Physics of Solids 54 (2006) 2592–2620.

[23] T. E. Oliphant, A. Manduca, R. L. Ehman, J. F. Greenleaf, Complex-valued stiffness reconstruction for magnetic resonance elastography by algebraic inversion of the differential equation, Magnetic Resonance in Medicine 45 (2) (2001) 299–310.

[24] P. J. McCracken, A. Manduca, J. Felmlee, R. L. Ehman, Mechanical transient-based magnetic resonance elastography, Magnetic Resonance in Medicine 53 (3) (2005) 628–639.

[25] E. E. Van Houten, M. M. Doyley, F. E. Kennedy, J. B. Weaver, K. D. Paulsen, Initial in vivo experience with steady-state subzone-based mr elastography of the human breast, Journal of Magnetic Resonance Imaging 17 (1) (2003) 72–85.

[26] I. Sack, J. Bernarding, J. Braun, Analysis of wave patterns in mr elastography of skeletal muscle using coupled harmonic oscillator simulations, Magnetic Resonance Imaging 20 (1) (2002) 95–104.

[27] A. T. Anderson, E. E. Van Houten, M. D. McGarry, K. D. Paulsen, J. L. Holtrop, B. P. Sutton, J. G. Georgiadis, C. L. Johnson, Observation of direction-dependent mechanical properties in the human brain with multi-excitation mr elastography, Journal of the Mechanical Behavior of Biomedical Materials 59 (2016) 538–546.

[28] J. Vappou, E. Breton, P. Choquet, C. Goetz, R. Willinger, A. Constantinesco, Magnetic resonance elastography compared with rotational rheometry for in vitro brain tissue viscoelasticity measurement, Magnetic Resonance Materials in Physics, Biology and Medicine 20 (5) (2007) 273–278.

[29] A. Jean, M. K. Nyein, J. Q. Zheng, D. F. Moore, J. D. Joannopoulos, R. Radovitzky, An animal-to-human scaling law for blast-induced traumatic brain injury risk assessment, Proceedings of the National Academy of Sciences 111 (43) (2014) 15310–15315.

[30] J. K. Shridharani, G. W. Wood, M. B. Panzer, B. P. Capeart, M. K. Nyein, R. A. Radovitzky, C. R. Bass, Porcine head response to blast, Frontiers in Neurology 3 (2012) 70.1–70.12.

[31] K. J. Glaser, A. Manduca, R. L. Ehman, Review of MR elastography applications and recent developments, Journal of Magnetic Resonance Imaging 36 (4) (2012) 757–774.

[32] J. A. W. van Dommelen, T. P. J. van der Sande, M. Hrapko, G. W. M. Peters, Mechanical properties of brain tissue by indentation: interregional variation, Journal of the Mechanical Behavior of Biomedical Materials 3 (2) (2010) 158–166.

[33] J. Zhang, M. A. Green, R. Sinkus, L. E. Bilston, Viscoelastic properties of human cerebellum using magnetic resonance elastography, Journal of Biomechanics 44 (10) (2011) 1909–1913.
[34] R. de Rooij, E. Kuhl, Constitutive modeling of brain tissue: current perspectives, Applied Mechanics Reviews 68 (1) (2016) 010801.
[35] S. Budday, G. Sommer, J. Hayback, P. Steinmann, G. Holzapfel, E. Kuhl, Rheological characterization of human brain tissue, Acta Biomaterialia (2017) doi:10.1016/j.actbio.2017.06.024.
[36] A. Mezer, J. D. Yeatman, N. Stikov, K. N. Kay, N.-J. Cho, R. F. Dougherty, M. L. Perry, J. Parvizi, L. H. Hua, K. Butts Pauly, B. A. Wandell, Quantifying the local tissue volume and composition in individual brains with magnetic resonance imaging, Nature Medicine 19 (12) (2013) 1667–1672.
[37] A. Gefen, S. S. Margulies, Are in vivo and in situ brain tissues mechanically similar?, Journal of Biomechanics 37 (9) (2004) 1339–1352.
[38] J. Vappou, E. Breton, P. Choquet, R. Willinger, A. Constantinesco, Assessment of in vivo and post-mortem mechanical behavior of brain tissue using magnetic resonance elastography, Journal of Biomechanics 41 (14) (2008) 2954–2959.
[39] A. Garo, M. Hrapko, J. Van Dommelen, G. Peters, Towards a reliable characterisation of the mechanical behaviour of brain tissue: the effects of post-mortem time and sample preparation, Biorheology 44 (1) (2007) 51–58.
[40] J. H. McElhaney, J. W. Melvin, V. L. Roberts, H. D. Portnoy, Dynamic characteristics of the tissues of the head, in: Perspectives in Biomedical Engineering, 1973, pp. 215–222.
[41] S. Nicolle, M. Lounis, R. Willinger, Shear properties of brain tissue over a frequency range relevant for automotive impact situations: new experimental results, Stapp Car Crash Journal 48 (2004) 239.
[42] S. Budday, R. Nay, R. de Rooij, P. Steinmann, T. Wyrobek, T. C. Ovaert, E. Kuhl, Mechanical properties of gray and white matter brain tissue by indentation, Journal of the Mechanical Behavior of Biomedical Materials 46 (2015) 318–330.
[43] K. Miller, K. Chinzei, G. Orssengo, P. Bednorz, Mechanical properties of brain tissue in-vivo: experiment and computer simulation, Journal of Biomechanics 33 (2000) 1369–1376.
[44] S. Saikali, P. Meurice, P. Sauleau, P.-A. Eliat, P. Bellaud, G. Randuineau, M. Vérin, C.-H. Malbert, A three-dimensional digital segmented and deformable brain atlas of the domestic pig, Journal of Neuroscience Methods 192 (1) (2010) 102–109.
[45] E. H. Clayton, G. M. Genin, P. V. Bayly, Transmission, attenuation and reflection of shear waves in the human brain, Journal of the Royal Society Interface 9 (76) (2012) 2899–2910.
[46] L. E. Bilston, Neural Tissue Biomechanics, Springer, Berlin Heidelberg, 2011.
[47] K. Miller, Biomechanics of the Brain, Springer, New York, 2011.
[48] K. Miller, K. Chinzei, Mechanical properties of brain tissue in tension, Journal of Biomechanics 35 (2002) 483–490.
[49] T. P. Prevost, G. Jin, M. A. De Moya, H. B. Alam, S. Suresh, S. Socrate, Dynamic mechanical response of brain tissue in indentation in vivo, in situ and in vitro, Acta Biomaterialia 7 (12) (2011) 4090–4101.
[50] G.-Y. Li, Y. Cao, Mechanics of ultrasound elastography, Proceedings of the Royal Society A 473 (2017) 20160841.
[51] A. Badachhape, R. Okamoto, R. Durham, B. Efron, S. Nadell, C. Johnson, P. Bayly, The relationship of three-dimensional human skull motion to brain tissue deformation in magnetic resonance elastography studies, Journal of Biomedical Engineering 139 (2017) 051002.
[52] I. E. Holm, A. K. O. Alstrup, Y. Luo, Genetically modified pig models for neurodegenerative disorders, Journal of Pathology 238 (2) (2016) 267–287.
[53] P. Sauleau, E. Lapouble, D. Val-Laillet, C.-H. Malbert, The pig model in brain imaging and neurosurgery, Animal 3 (08) (2009) 1138–1151.
[54] S. Eaton, T. Wishart, Bridging the gap: large animal models in neurodegenerative research, Mammalian Genome (2017) 1–14.